Pergamon

PII: S0045-7949(97)00036-9

Computers & Structures Vol. 64, No. 5/6, pp. 1069–1085, 1997

Printed in Great Britain
0045-7949/97 $17.00 + 0.00

ON THE CONSTRAINT FUNCTION METHOD FOR CONTACT PROBLEMS

K. J. Bathe† and **P. A. Bouzinov‡**

†Massachusetts Institute of Technology, Cambridge, MA, U.S.A.
‡ADINA R & D, Inc., Watertown, MA, U.S.A.

Abstract—The objective in this paper is to present some theoretical insight and valuable numerical experiences for the analysis of contact problems. We review the theoretical basis of the constraint function method for general contact problems and discuss some important characteristics of the method. In the presentation, we consider static and dynamic conditions. We then give numerical experiences with the method through the solution of some demonstrative test problems and through the results obtained in some industrial analysis cases. © 1997 Elsevier Science Ltd.

1. INTRODUCTION

There are many physical situations in which contact between bodies represents a significant phenomenon and must be included in a refined stress analysis. Contact problems range from frictionless contact with infinitesimally small displacements to contact with friction in large strain conditions. Hence, the contact conditions may be rather simple to include in the finite element analysis or may represent strong nonlinearities that require a powerful analysis procedure.

We have developed the constraint function method for contact analysis which can be employed effectively for many contact problems [1, 2]. The method has some advantages over other available techniques, but few numerical experiences have been published.

The objective in this paper is to review the theoretical basis of the constraint function method for the analysis of contact problems, to give theoretical insight into the method, and in particular to present numerical experiences with the procedure. The numerical solutions that we present using the contact algorithm pertain to some demonstrative test problems and to industrial analysis cases.

In the next sections, we first present the theoretical basis of the constraint function method for static and dynamic contact solutions (using implicit time integration), and then present some numerical results and experiences obtained with the method.

2. CONTACT CONDITIONS

Without loss of generality, let us consider two bodies in contact, see Fig. 1. The developments given below can, of course, be directly extended to multiple body contact conditions. The principle of virtual work governing the conditions of the two bodies in the deformed configuration at time t is:

$$\sum_{L=1}^{2}\int_{{}^{t}V} {}^{t}\tau_{ij}\,\delta_t e_{ij}\,\mathrm{d}^tV = \sum_{L=1}^{2}\left\{\int_{{}^{t}V}\delta u_i\,{}^{t}f_i^B\,\mathrm{d}^tV + \int_{{}^{t}S_f}\delta u_i^S\,{}^{t}f_i^S\,\mathrm{d}^tS\right\} + \sum_{L=1}^{2}\int_{{}^{t}S_c}\delta u_i^c\,{}^{t}f_i^c\,\mathrm{d}^tS \quad (1)$$

where, for each body I and J, ${}^tV$ is the volume of the body, ${}^t\tau_{ij}$ are the components of the Cauchy stress tensor, $\delta_t e_{ij}$ are the virtual strain components corresponding to the virtual imposed displacements δu_i, ${}^tf_i^B$ are the components of the externally applied force per unit volume, ${}^tf_i^S$ are the components of the known externally applied surface tractions, and ${}^tf_i^c$ are the components of the unknown contact tractions. Note that for each body, the known surface tractions act on the surface area ${}^tS_f$ and the unknown contact tractions act on the unknown and to be calculated area ${}^tS_c$.

Figure 1 illustrates schematically how bodies I and J are in contact at time t. Note that (for a static analysis) each body is supported such that without contact, no rigid body motion is possible. Let ${}^t\mathbf{f}^{IJ}$ be the vector of contact surface tractions on the body I due to contact with body J, then ${}^t\mathbf{f}^{IJ} = -{}^t\mathbf{f}^{JI}$. Hence, the virtual work due to the contact tractions in eqn (1) can be written as:

$$\int_{S^{IJ}}\delta u_i^I\,{}^tf_i^{IJ}\,\mathrm{d}S^{IJ} + \int_{S^{JI}}\delta u_i^J\,{}^tf_i^{JI}\,\mathrm{d}S^{JI} = \int_{S^{IJ}}\delta u_i^{IJ}\,{}^tf_i^{IJ}\,\mathrm{d}S^{IJ} \quad (2)$$

where δu_i^I and δu_i^J are the components of the virtual

displacements on the contact surfaces of bodies I and J respectively, and

$$\delta u_i^{IJ} = \delta u_i^I - \delta u_i^J . \tag{3}$$

We call the pair of surfaces S^{IJ} and S^{JI} a 'contact surface pair' and note that these surfaces are not necessarily of equal size. However, the actual area of contact at time t for body I is ${}^tS_c$ of body I and for body J is ${}^tS_c$ of body J, and in each case this area is part of S^{IJ} and S^{JI} (see Fig. 1). It is convenient to call S^{IJ} the 'contactor surface' and S^{JI} the 'target surface.' Hence, the right-hand side of eqn (2) can be interpreted as the virtual work that the contact tractions produce corresponding to the virtual relative displacements for the contact surface pair.

In the following we analyze the right-hand side of eqn (2). Let $\mathbf{n}$ be the unit outward normal to S^{JI} and let $\mathbf{s}$ be a vector such that $\mathbf{n}, \mathbf{s}$ form a right-hand basis, see Fig. 2. We can decompose the contact tractions ${}^t\mathbf{f}^{IJ}$ acting on S^{IJ} into normal and tangential components corresponding to $\mathbf{n}$ and $\mathbf{s}$ on S^{JI},

$${}^t\mathbf{f}^{IJ} = \lambda \mathbf{n} + t\mathbf{s} \tag{4}$$

where λ and t are the normal and tangential traction components (for brevity of notation we do not use a

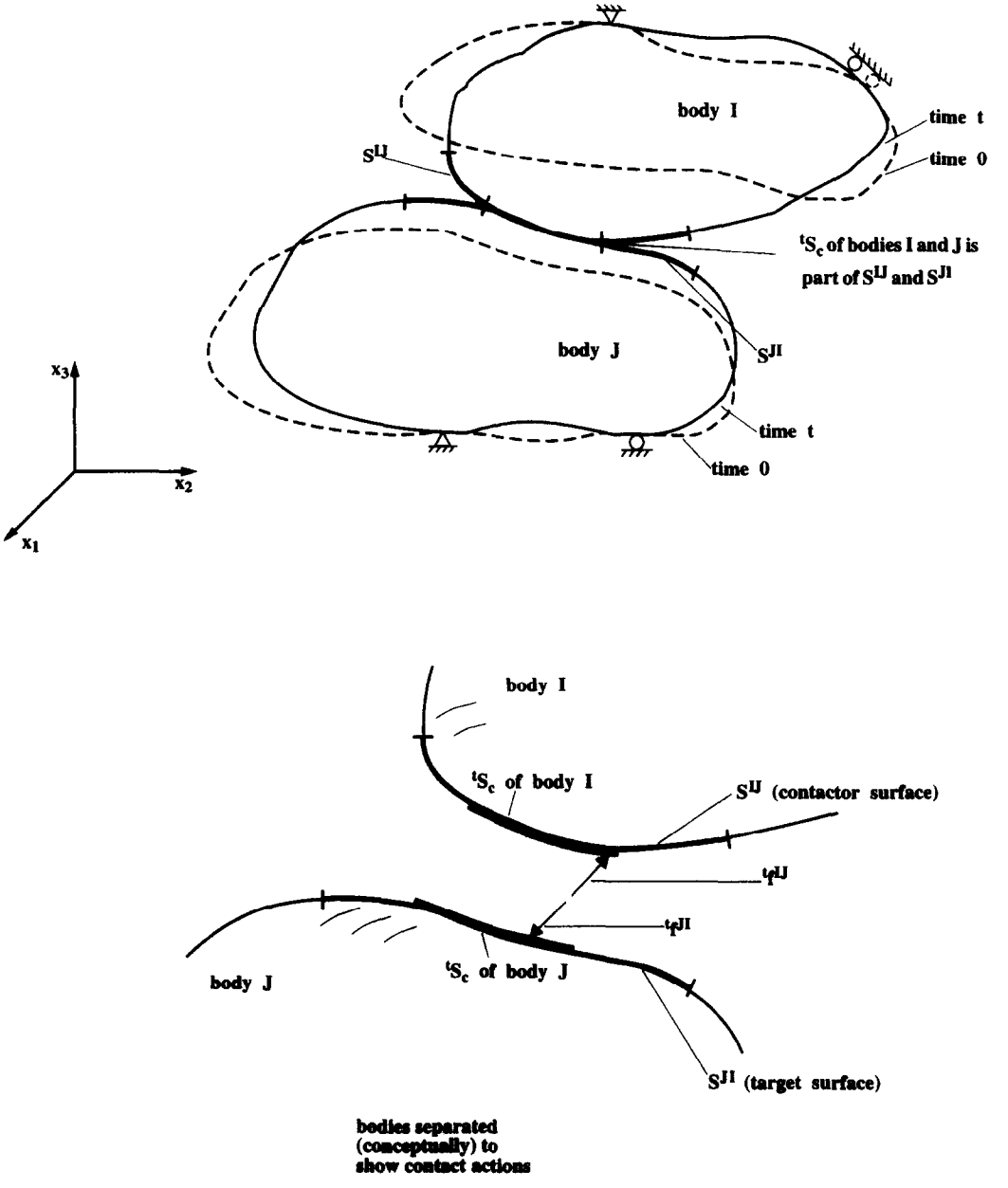

Fig. 1. Bodies in contact at time t.

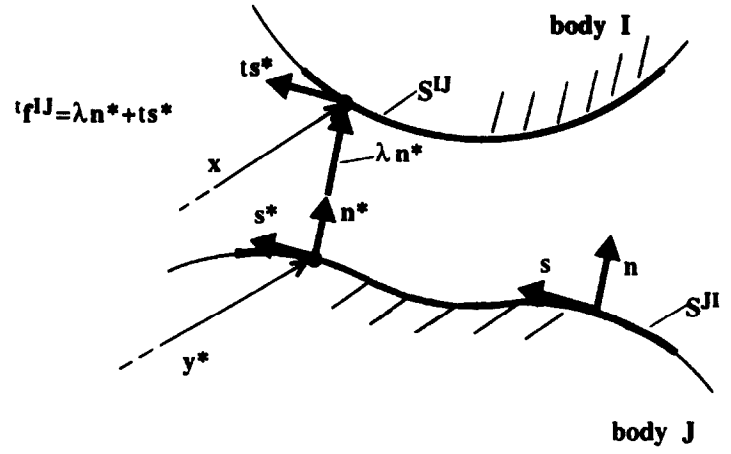

Fig. 2. Definition of contact quantities.

superscript). Hence,

$$\lambda = ({}^t\mathbf{f}^{IJ})^T\mathbf{n};\ t = ({}^t\mathbf{f}^{IJ})^T\mathbf{s}\,. \tag{5}$$

To define the actual values of $\mathbf{n}$, $\mathbf{s}$ that we use in our contact calculations, consider a generic point $\mathbf{x}$ at time t on S^{IJ} and let $\mathbf{y}^*(\mathbf{x},t)$ be the point on S^{JI} satisfying:

$$\|\mathbf{x} - \mathbf{y}^*(\mathbf{x},t)\|_2 = \min_{\mathbf{y}\in S^{JI}}\left\{\|\mathbf{x} - \mathbf{y}\|_2\right\}. \tag{6}$$

The (signed) distance from $\mathbf{x}$ to S^{JI} is then given by:

$$g(\mathbf{x},t) = (\mathbf{x} - \mathbf{y}^*)^T\mathbf{n}^* \tag{7}$$

where $\mathbf{n}^*$ is the unit 'normal vector' that we use at $\mathbf{y}^*(\mathbf{x},t)$ (see Fig. 2). The vectors $\mathbf{n}^*$, $\mathbf{s}^*$ are used in eqn (4) corresponding to the point $\mathbf{x}$. The function g is the gap function for the contact surface pair.

With these definitions, the conditions for normal contact can now be written as:

$$g \geq 0;\ \lambda \geq 0;\ g\lambda = 0 \tag{8}$$

where the last equation expresses the fact that if $g > 0$, then we must have $\lambda = 0$, and vice versa.

To include frictional conditions, let us assume that Coulomb's law of friction holds pointwise on the contact surface and that μ is the coefficient of friction. This assumption means of course that frictional effects are included in a very simplified manner (for more details see, for example [3, 4]).

Let us define the nondimensional variable τ given by

$$\tau = \frac{t}{\mu\lambda};\ \lambda > 0 \tag{9}$$

where $\mu\lambda$ is the 'frictional resistance' and the magnitude of the relative tangential velocity

$$\dot{u}(\mathbf{x},t) = (\dot{\mathbf{u}}^I|_{\mathbf{y}^*(\mathbf{x},t)} - \dot{\mathbf{u}}^I|_{(\mathbf{x},t)})^T\mathbf{s}^* \tag{10}$$

corresponding to the unit tangential vector $\mathbf{s}$ at $\mathbf{y}^*(\mathbf{x},t)$. Hence $\dot{u}(\mathbf{x},t)\mathbf{s}^*$ is the tangential velocity at time t of the material point at $\mathbf{y}^*$ relative to the material point at $\mathbf{x}$. With these definitions, Coulomb's law of friction states

$$|\tau| \leq 1$$

and

$$|\tau| < 1 \text{ implies } \dot{u} = 0 \tag{11}$$

while

$$|\tau| = 1 \text{ implies } \operatorname{sign}(\dot{u}) = \operatorname{sign}(\tau)$$

Figure 3 illustrates these interface conditions.

The solution of the contact problem in Fig. 1 therefore entails the solution of the virtual work eqn (1) subject to the conditions in eqns (8) and (11).

In the above equations, we considered the equilibrium, compatibility and stress–strain conditions at a generic time t. If the body force components ${}^tf_i^B$ include inertia and damping forces, the above equations are also applicable in dynamic analysis (although the simple Coulomb friction law used is then even more approximate than in static analysis). However, in dynamic analysis, not only must the displacements be compatible at the contact surface, but also the velocities and accelerations. These additional requirements are fulfilled using a special treatment in the numerical solution as mentioned in Section 4.

3. THE CONSTRAINT FUNCTION METHOD

The conditions to be satisfied in contact analysis are given in eqns (8),(11). In the constraint function method, we use a function $w(g,\lambda)$ such that when

$w(g,\lambda) = 0$, the conditions in eqn (8) are satisfied. It is important to note that $w(g,\lambda)$ is to be a continuous and differentiable function for *all* values of λ and g, because in such a case, we can establish the appropriate derivatives in the Newton–Raphson iteration to satisfy $w(g,\lambda) = 0$. A reasonable function is obtained by using the regularization

$$\lambda = \frac{\epsilon_n}{g} \tag{12}$$

for the normal contact condition in Fig. 3, where $\epsilon_n \ll 1$. The w function is constructed to be zero at the values given in eqn (12), positive in the first quadrant and negative in the other three quadrants. We obtain:†

$$w(g,\lambda) = \frac{g+\lambda}{2} - \sqrt{\left(\frac{g-\lambda}{2}\right) + \epsilon_n} \tag{13}$$

The same approach is employed to impose the frictional conditions. Namely, let $v(\dot{u},\tau)$ be a continuous and differentiable function such that when $v(\dot{u},\tau) = 0$, the conditions in eqn (11) are satisfied. To construct the function we use instead of eqn (11) the following relationship:

$$\tau = \frac{2}{\pi} \arctan \frac{\dot{u}}{\epsilon_\tau} \tag{14}$$

where $\epsilon_\tau \ll 1$. Here we can interpret ϵ_τ to be a physical parameter representing a characteristic behavior in the friction law.

The constraint function method now consists of solving eqn (1) (using the usual finite element discretization schemes) and imposing the conditions

$$w(g,\lambda) = 0 \tag{15}$$

†In practice, g and λ would be used in nondimensional form.

and

$$v(\dot{u},\tau) = 0 \tag{16}$$

onto the solution. These constraints can be imposed using a penalty or Lagrange multiplier method [1]. We have chosen to use, in the ADINA implementation, the Lagrange multiplier method because in this case, no (artificial) penalty parameter need be chosen which can result into ill-conditioning of the coefficient matrix obtained upon discretization.

Considering the variables λ and τ as Lagrange multipliers, the constraint equation for the continuum is:

$$\int_{S^{IJ}} [\delta\lambda\, w(g,\lambda) + \delta\tau\, v(\dot{u},\tau)] \mathrm{d}S^{IJ} = 0 \tag{17}$$

which must be solved in addition to eqn (1) (with the contact force term unknown as in eqn (2)).

4. FINITE ELEMENT DISCRETIZATION

The finite element discretization of the bodies in contact is achieved using the standard procedures of interpolation [1]. However, special considerations are necessary in the discretization of the contact conditions.

Consider, in the incremental analysis, the governing equations at time $t + \Delta t$. The contact traction term in eqn (1) will clearly result into nodal point forces, the vector of which we call ${}^{t+\Delta t}\mathbf{R}_c$ and the constraint equations in eqns (15) and (16) will result in a vector of constraints. Assume that we assign at each node k of the contactor surface S^{IJ}, a pair of unknowns ${}^{t+\Delta t}\lambda_k$ and ${}^{t+\Delta t}\tau_k$. These discrete Lagrange multiplier values are used to impose the contact constraints. Then, following our usual notation [1],

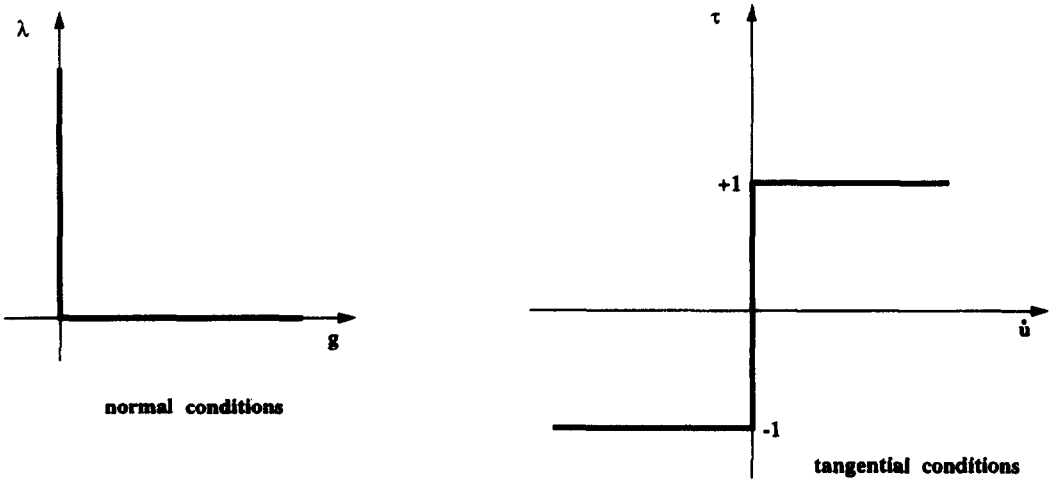

Fig. 3. Interface conditions in contact analysis.

the governing equations are, at time $t + \Delta t$:

$$ {}^{t+\Delta t}\mathbf{F}({}^{t+\Delta t}\mathbf{U}) = {}^{t+\Delta t}\mathbf{R} - {}^{t+\Delta t}\mathbf{R}_c({}^{t+\Delta t}\mathbf{U}, {}^{t+\Delta t}\tau) \quad (18) $$

and

$$ {}^{t+\Delta t}\mathbf{F}_c({}^{t+\Delta t}\mathbf{U}, {}^{t+\Delta t}\tau) = \mathbf{0} \quad (19) $$

where, with m contactor nodes,

$$ {}^{t+\Delta t}\tau^T = $$
$$ [{}^{t+\Delta t}\lambda_1, {}^{t+\Delta t}\tau_1, \cdots, {}^{t+\Delta t}\lambda_k, {}^{t+\Delta t}\tau_k, \cdots, {}^{t+\Delta t}\lambda_m, {}^{t+\Delta t}\tau_m] \,. \quad (20) $$

Note that the relative velocity and gap functions are of course expressed in terms of the nodal point displacements.

The vector ${}^{t+\Delta t}\mathbf{F}_c$ can be written as

$$ {}^{t+\Delta t}\mathbf{F}_c^T = [{}^{t+\Delta t}\mathbf{F}_1^{cT}, \cdots, {}^{t+\Delta t}\mathbf{F}_m^{cT}] \quad (21) $$

where we use, with proper normalizations,

$$ {}^{t+\Delta t}\mathbf{F}_k^c = \begin{bmatrix} w({}^{t+\Delta t}g_k, {}^{t+\Delta t}\lambda_k) \\ v({}^{t+\Delta t}\dot{u}_k, {}^{t+\Delta t}\tau_k) \end{bmatrix} . \quad (22) $$

The incremental equations for the solution of eqns (18) and (19) are obtained by linearization about the last calculated state. Following the usual procedures [1], the resulting equations corresponding to the linearization about the state at time t are

$$ \begin{bmatrix} ({}^t\mathbf{K} + {}^t\mathbf{K}_{uu}^c) & {}^t\mathbf{K}_{u\tau}^c \\ {}^t\mathbf{K}_{\tau u}^c & {}^t\mathbf{K}_{\tau\tau}^c \end{bmatrix} \begin{bmatrix} \Delta\mathbf{U} \\ \Delta\tau \end{bmatrix} = \begin{bmatrix} {}^{t+\Delta t}\mathbf{R} - {}^t\mathbf{F} - {}^t\mathbf{R}_c \\ - {}^t\mathbf{F}_c \end{bmatrix} \quad (23) $$

where $\Delta\mathbf{U}$ and $\Delta\tau$ are the increments in the solution variables ${}^t\mathbf{U}$ and ${}^t\tau$, and ${}^t\mathbf{K}_{uu}^c$, ${}^t\mathbf{K}_{u\tau}^c$, ${}^t\mathbf{K}_{\tau u}^c$ and ${}^t\mathbf{K}_{\tau\tau}^c$ are contact stiffness matrices

$$ \left.\begin{aligned} {}^t\mathbf{K}_{uu}^c &= \frac{\partial {}^t\mathbf{R}_c}{\partial {}^t\mathbf{U}}; \quad {}^t\mathbf{K}_{u\tau}^c = \frac{\partial {}^t\mathbf{R}_c}{\partial {}^t\tau} \\ {}^t\mathbf{K}_{\tau u}^c &= \frac{\partial {}^t\mathbf{F}_c}{\partial {}^t\mathbf{U}}; \quad {}^t\mathbf{K}_{\tau\tau}^c = \frac{\partial {}^t\mathbf{F}_c}{\partial {}^t\tau} \end{aligned}\right\} \quad (24) $$

Of course, in practice, a Newton–Raphson iteration is performed, in which the above linearization is carried out in preassigned iterations. We usually use the full Newton–Raphson method [1], and a valuable feature is also that line searching can directly be employed with this contact solution algorithm. Line searching can be important when contact with elasto-plasticity or large deformations is solved.

The above spatial discretization is applicable to static and dynamic analysis. However, in dynamic analysis some additional considerations are necessary. Consider the dynamic equilibrium equation at time $t + \Delta t$:

$$ \mathbf{M}\,{}^{t+\Delta t}\ddot{\mathbf{U}} + {}^{t+\Delta t}\mathbf{F}({}^{t+\Delta t}\mathbf{U}) = {}^{t+\Delta t}\mathbf{R} - {}^{t+\Delta t}\mathbf{R}_c({}^{t+\Delta t}\mathbf{U}, {}^{t+\Delta t}\tau) \quad (25) $$

which is eqn (18) with the inertia forces added (or rather extracted from the body force components ${}^{t+\Delta t}f_i^B$; the damping forces would be included in a similar manner). Equation (19) still ensures that the displacement contact compatibility requirements are satisfied.

The difficulty lies in the numerical time integration using, for example, the trapezoidal rule for eqn (25). Assume that the time integration scheme solves for the unknown displacements using eqns (25) and (19). The incremental displacements will then, after contact has been initiated, lead to a compatible displacement field, but the velocities and accelerations are not necessarily identical for the contactor and target surfaces. This is only achieved if post-impact conditions are imposed that ensure the compatibility of the velocities and accelerations as well.

The post-impact conditions we use are that the momentum and the time derivative thereof, for the masses at the contactor and target surfaces, are preserved. These conditions mean that some kinetic energy is lost on impact, but the amount of this energy loss is small when fine finite element discretizations are used in the solution.

5. SAMPLE SOLUTIONS

We present the following example solutions in order to demonstrate the applicability of the constraint function algorithm for complex contact problems. All these solutions have been obtained with the ADINA program, version 7.1. An additional complex contact analysis is presented in Ref. [5].

5.1. *Sliding of rubber block in a channel*

This plane-stress static problem was studied in Ref. [6] because it represents a valuable test problem for a contact algorithm. Figure 4 shows the rubber block and finite element idealization used. The right face of the block is subjected to the displacement history given in the figure making this a large deformation problem.

The solution using the Coulomb friction coefficient $\mu = 0.15$ is presented in Fig. 5. The friction constraint function parameter $\epsilon_\tau = 0.001$ was employed and the normal constraint function parameter ϵ_n was computed automatically to be small in comparison with g and λ. The solution given compares well with the solution presented in Ref. [6].

5.2. *Pressing of thin steel plates*

Two circular thin steel plates are pressed into a rigid die. Figure 6 shows the axisymmetric geometry of the plates, punch and blank holder, and the

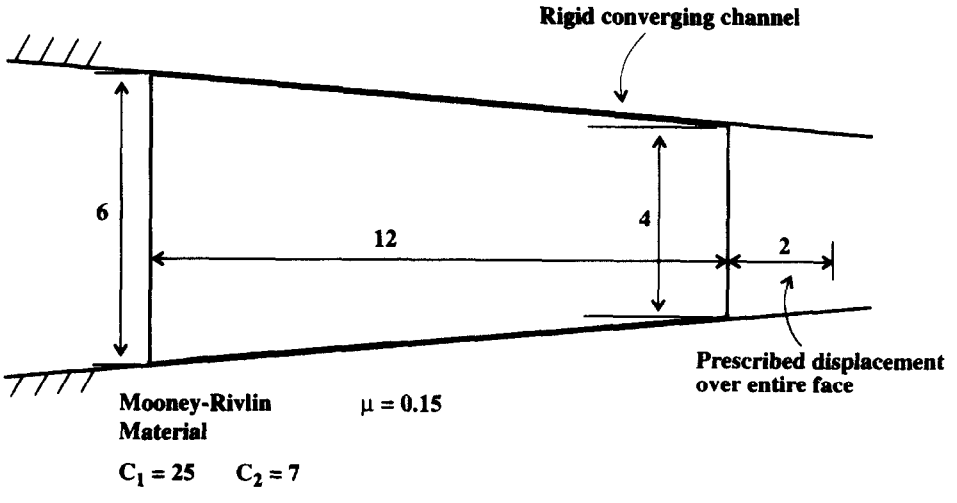

(a) Problem considered

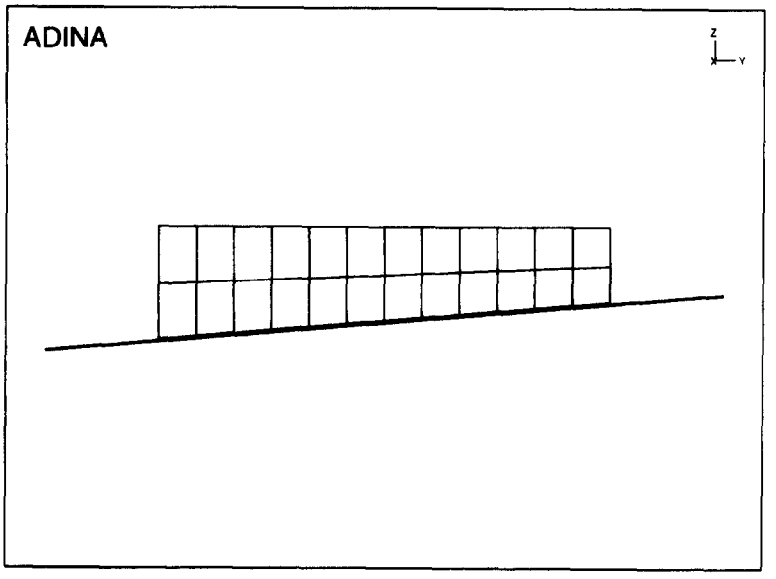

(b) 4-node element mesh used for half of sheet

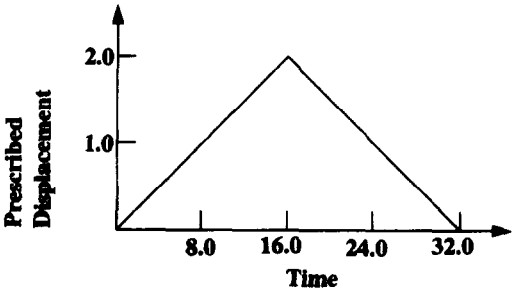

(c) Prescribed displacement

Fig. 4. Analysis of rubber block: (a) problem considered; (b) four-node element mesh used for half of sheet; (c) prescribed displacement.

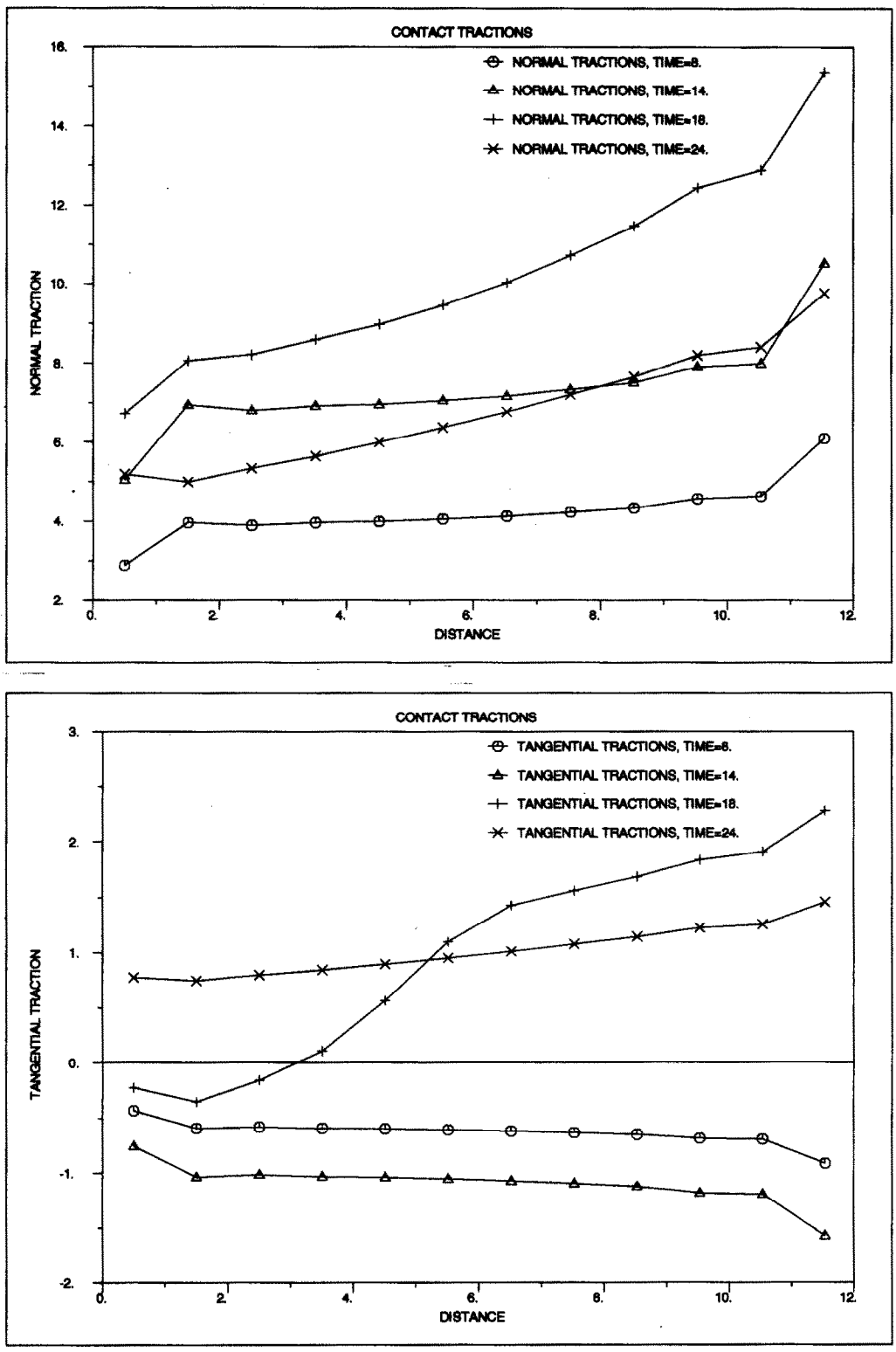

Fig. 5. Contact tractions at different times in rubber block solution.

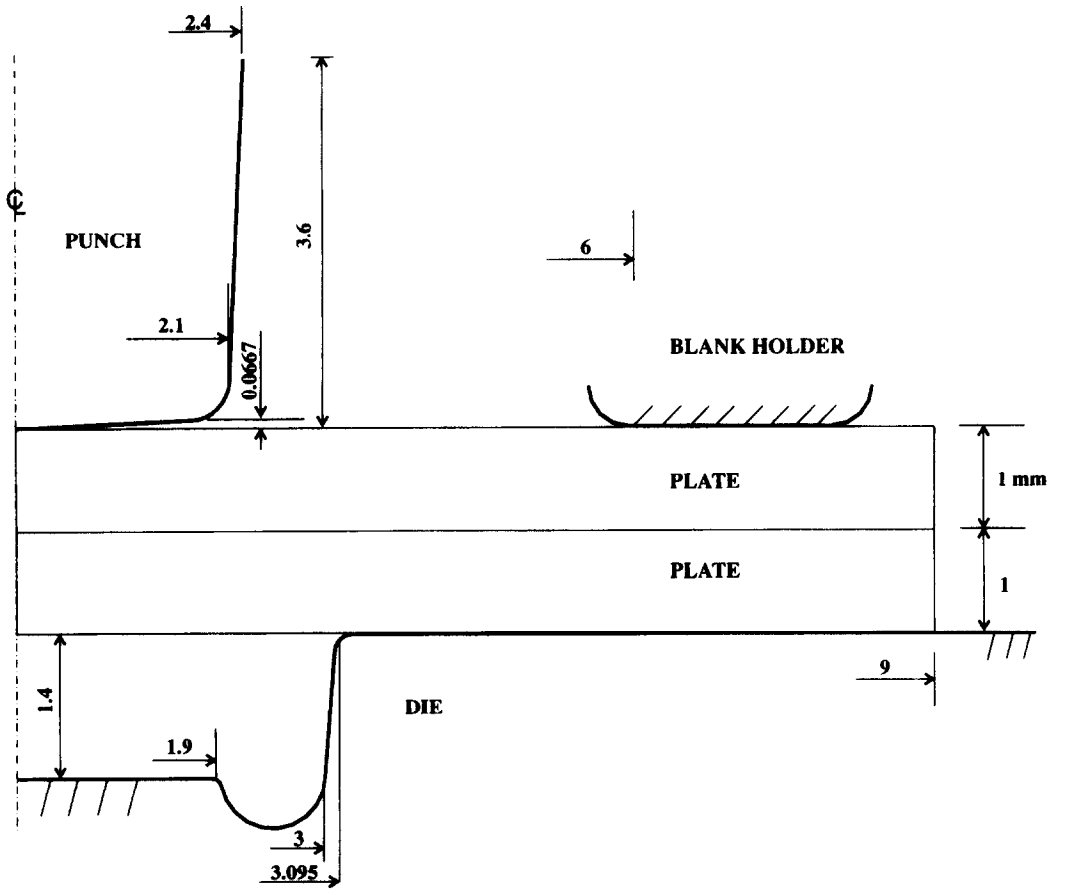

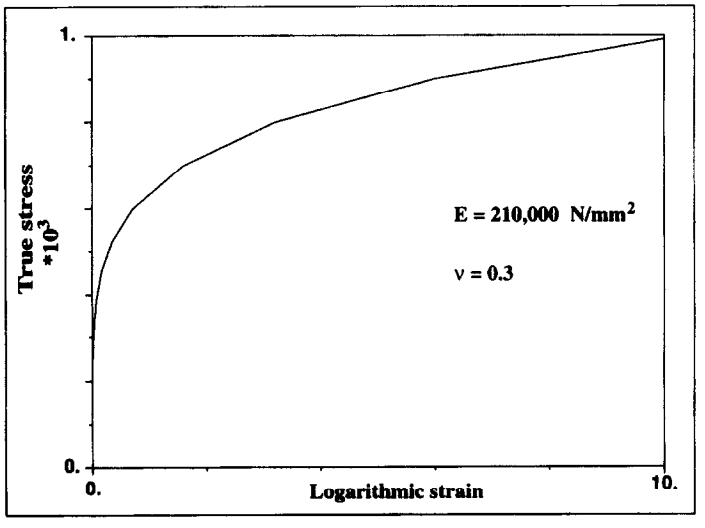

Fig. 6. Geometry and stress–strain relationship in analysis of pressed steel plates.

elasto-plastic stress–strain relationship of the plate material. Contact with no friction was assumed.

Figure 7 shows the finite element model used with ADINA. Various deformed configurations calculated during the solution process are given in Fig. 8. The final punch displacement was reached in 152 load steps, automatically adjusted in magnitudes in ADINA.

The calculated vertical force–punch displacement relationship is presented in Fig. 9. The accumulated effective plastic strain in the lower plate near the center line is, in the final configuration, larger than

500%. Note also the wrinkle developing in the upper surface of the lower plate.

5.3. *Analysis of rubber boot*

Figure 10 shows the finite element model of the rubber boot analyzed; due to symmetry conditions only one-half of the structure is considered. The boot has a maximum radius of 46.3 mm and a height of 96 mm. The wall thickness varies from 6.35 mm (at the fixed end) to about 2.5 mm (in the deformable part). The material behavior is modeled using the Mooney–Rivlin model with $C_1 = 0.053$ N mm^{-2}, $C_2 = 0.01$ N mm^{-2} and the bulk modulus equal to 10 N mm^{-2}. The stick shift material is steel. A maximum rotation of 40° is applied to the stick shift.

The finite element model was prepared originally using I-DEAS with which a mesh of 20-node three-dimensional elements was generated. However, for an almost incompressible analysis, it is much more effective to employ 27-node elements [1]. Therefore, we used the TRANSOR program to convert all 20-node elements to 27-node elements, so that the 27/4 displacement/pressure element could be employed. Frictionless contact was assumed; the contact surfaces are shown by thick lines in Fig. 10. Note that the contact will include self-contact on the rubber part, i.e. this contact surface can come into contact with itself.

The final deformed configuration is given in Fig. 11, which shows the large deformations in the rubber and that wrinkles have developed.

5.4. *Cutting of rock*

A stiff elastic cutting tooth is cutting into a rock mass. First, the tooth moves down into the negative y-direction and then it moves into the z-direction (see Fig. 12). The rock mass was modeled as an elasto-plastic material with rupture at an effective strain of 0.02. The tooth geometry was established in Pro/E and meshed in ADINA (see Fig. 13), using four-node tetrahedral elements.

Figure 14 displays the final configuration of the tooth in the rock. The figure shows how the cutting tool has penetrated the rock. We note that the finite elements around the tool have ruptured (these elements are no longer present in the rock mass).

5.5. *Impact of two pipes*

Two steel pipes impact upon each other, see Fig. 15. The upper pipe moves with an initial velocity in the z-direction corresponding to an angular velocity of 75 rad s^{-1} about its right end. Frictionless contact is assumed.

The analysis was conducted using symmetry conditions for the pipes. Figures 15(b) and 16 show the meshes of four-node MITC elements used for the pipes, and the calculated configuration at a time of 0.01 s. The trapezoidal rule of time integration was

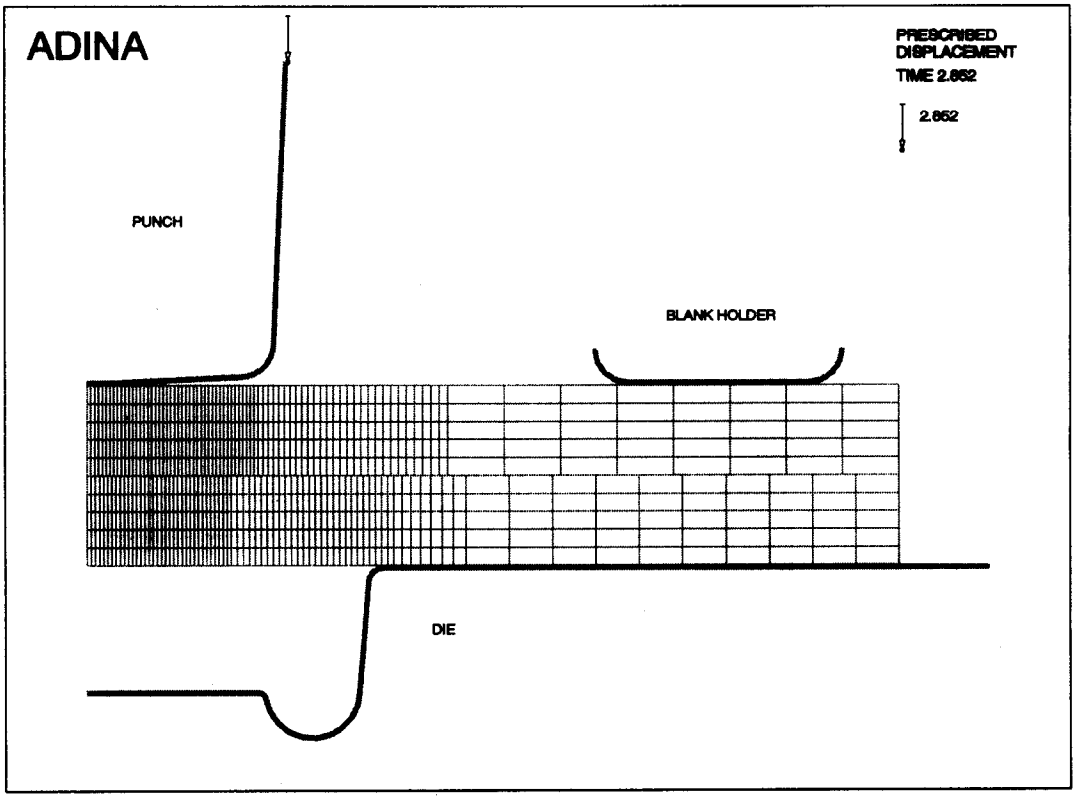

Fig. 7. Finite element model of plates.

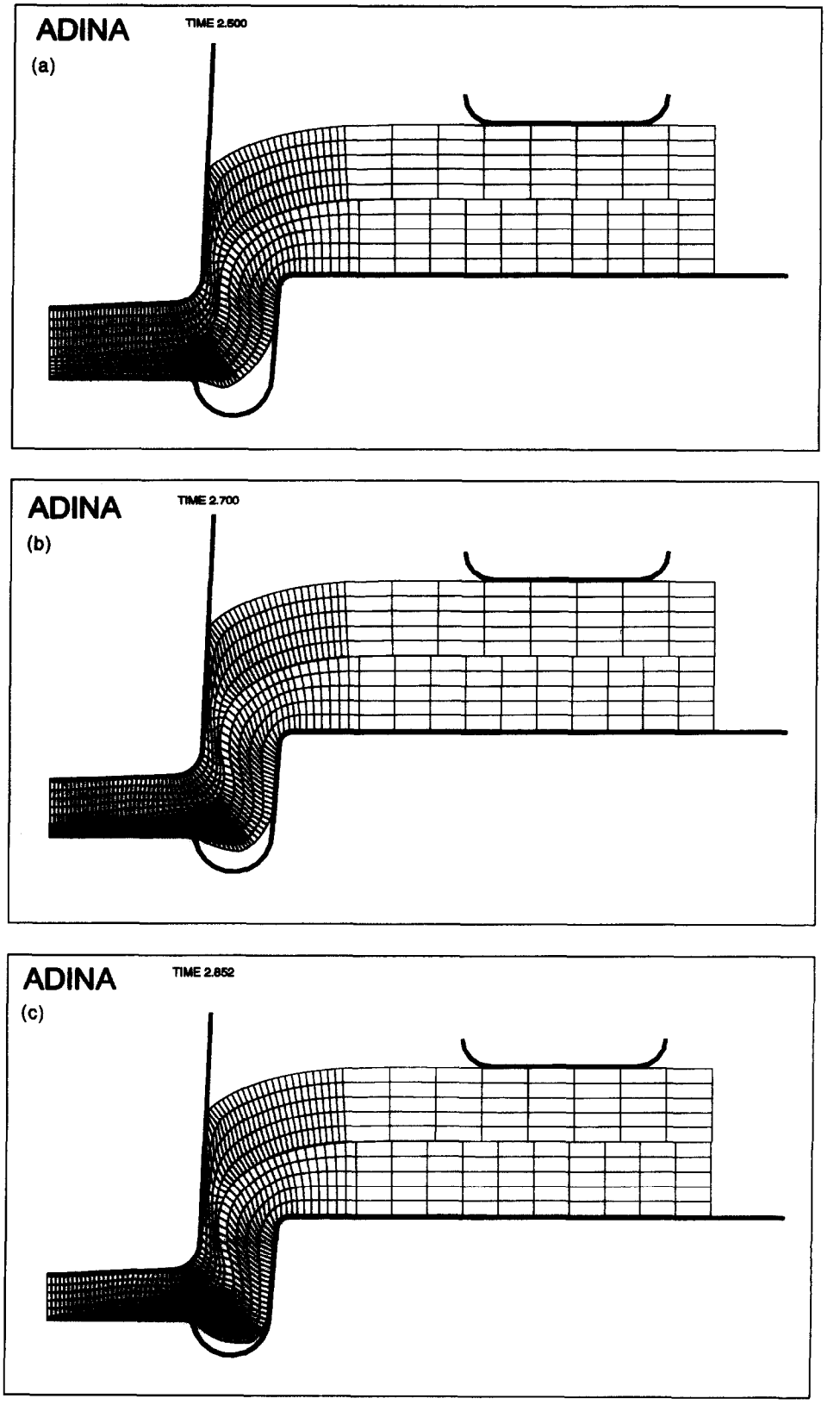

Fig. 8. Deformed configurations of plates: (a) at displacement of 2.5 mm; (b) at displacement of 2.7 mm; (c) at displacement of 2.852 mm (final configuration).

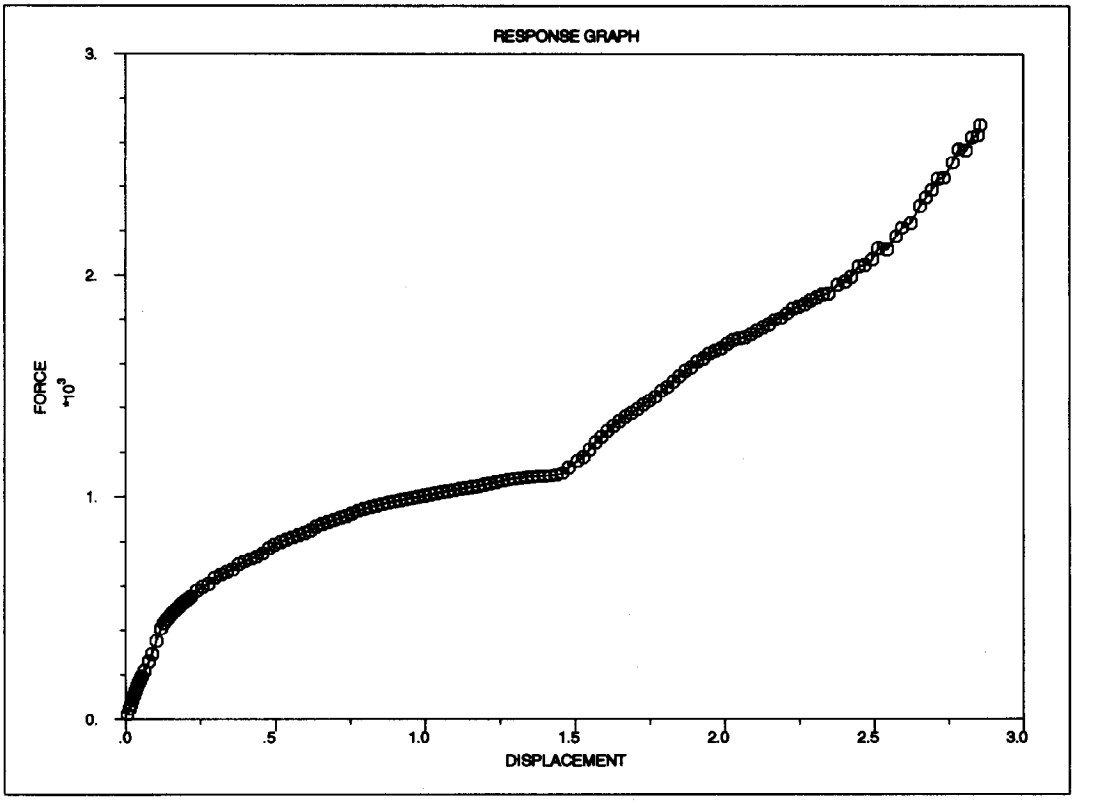

Fig. 9. The calculated punch force–displacement curve for one radian of structure in the analysis of the pressed steel plates.

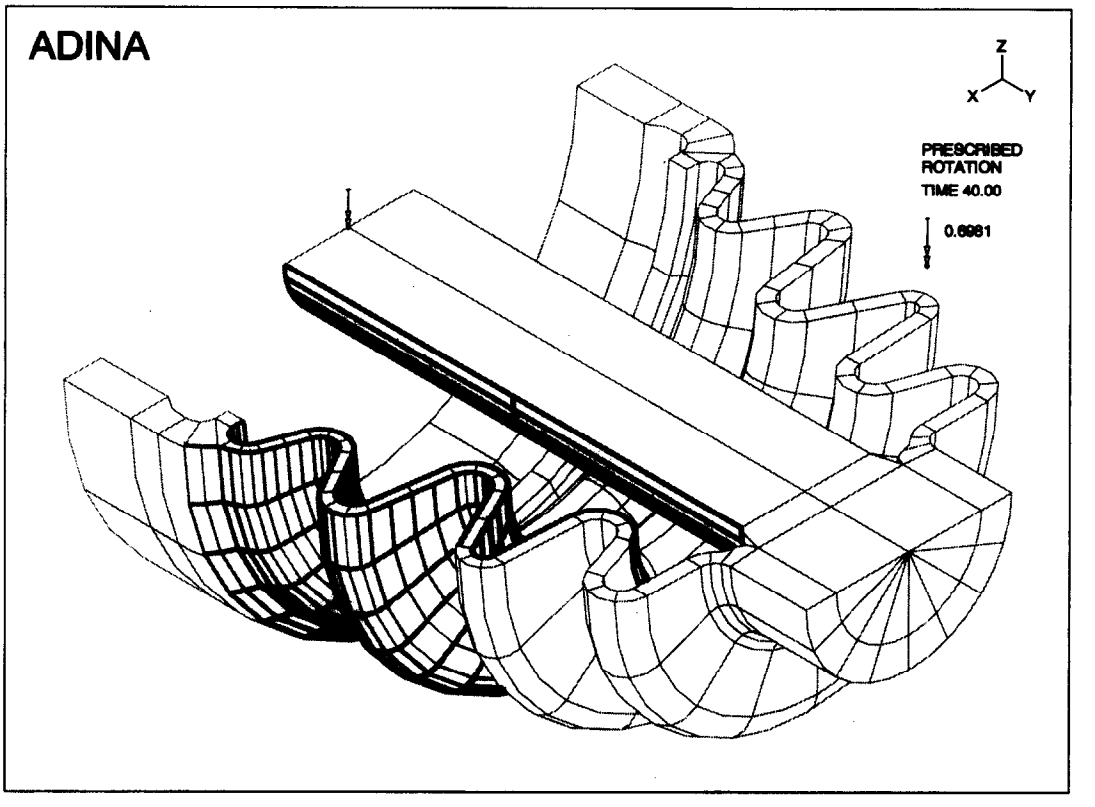

Fig. 10. Rubber boot finite element model.

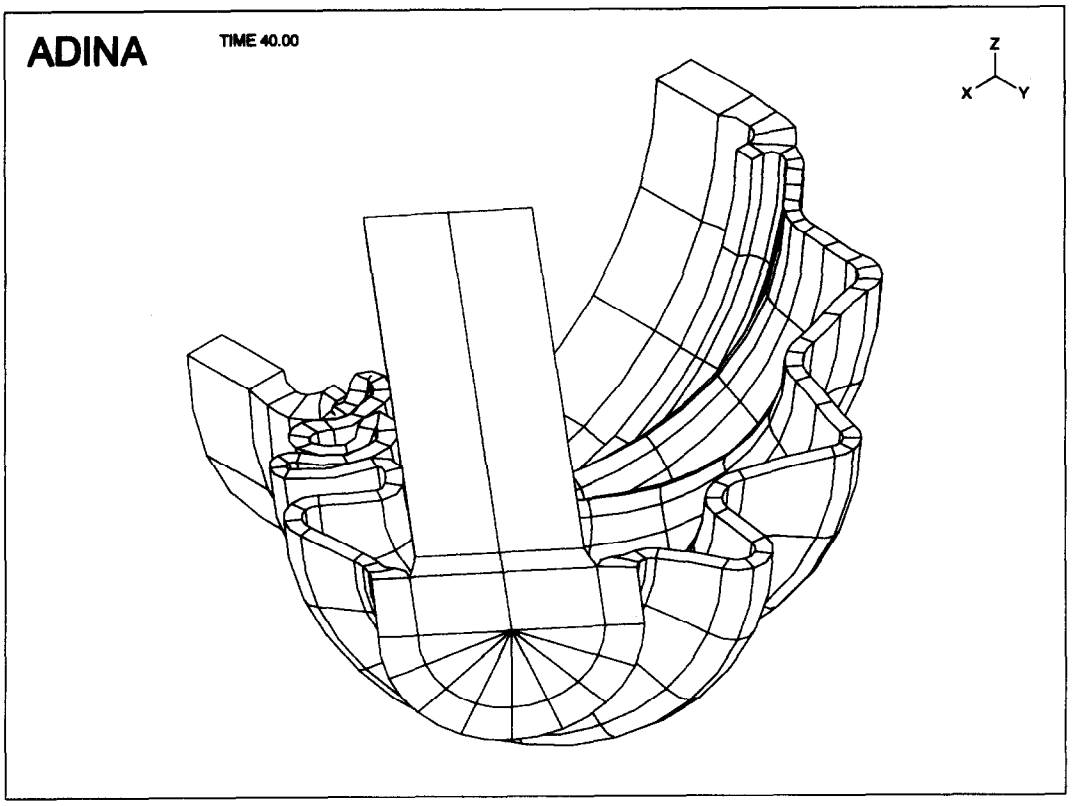

Fig. 11. Final deformed rubber boot configuration.

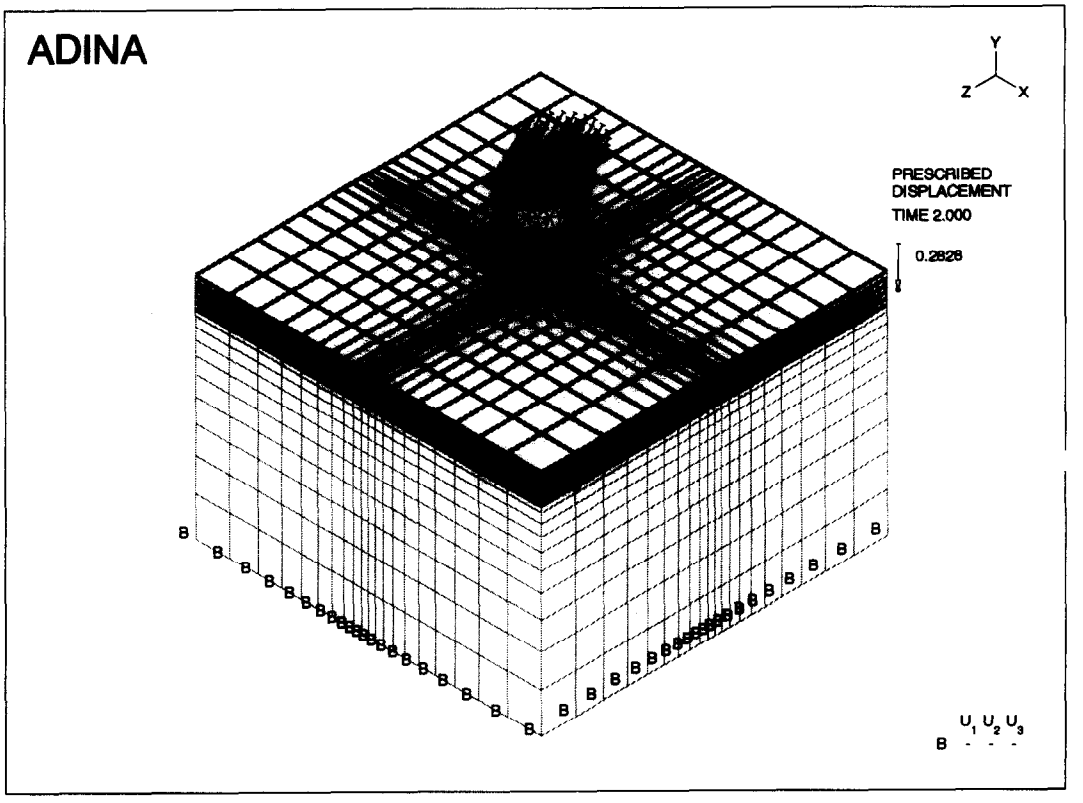

Fig. 12. Finite element model of tooth cutting into rock.

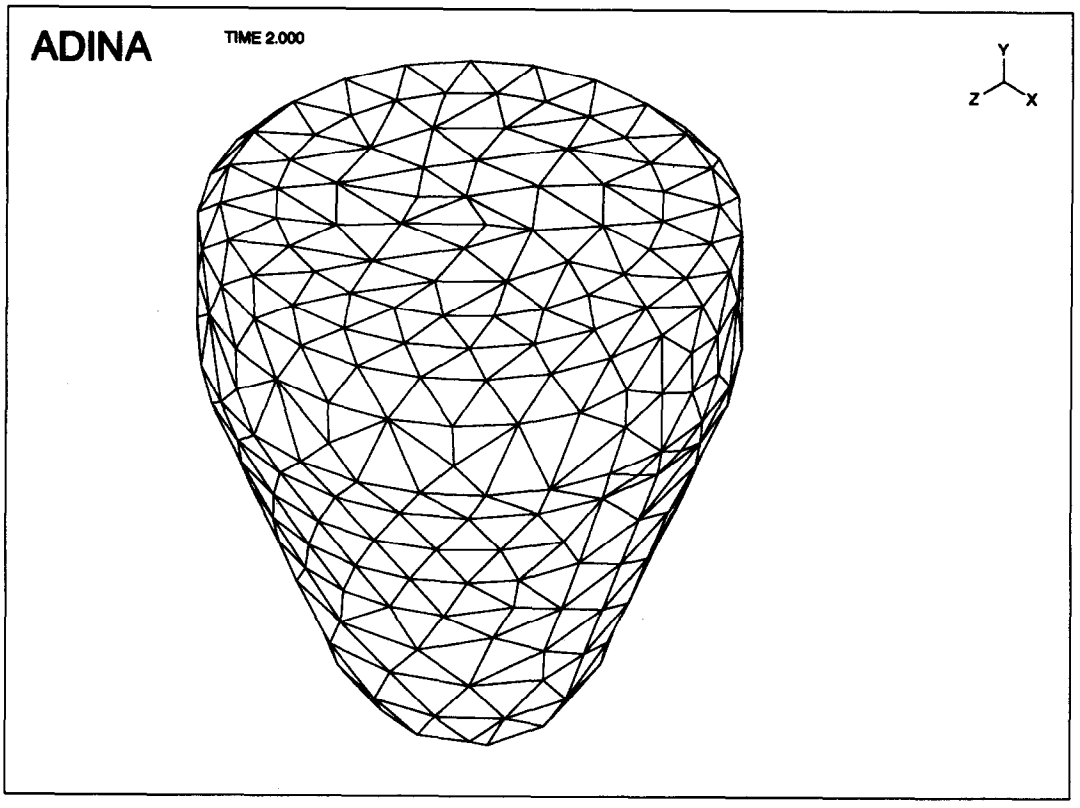

Fig. 13. The model of the tooth.

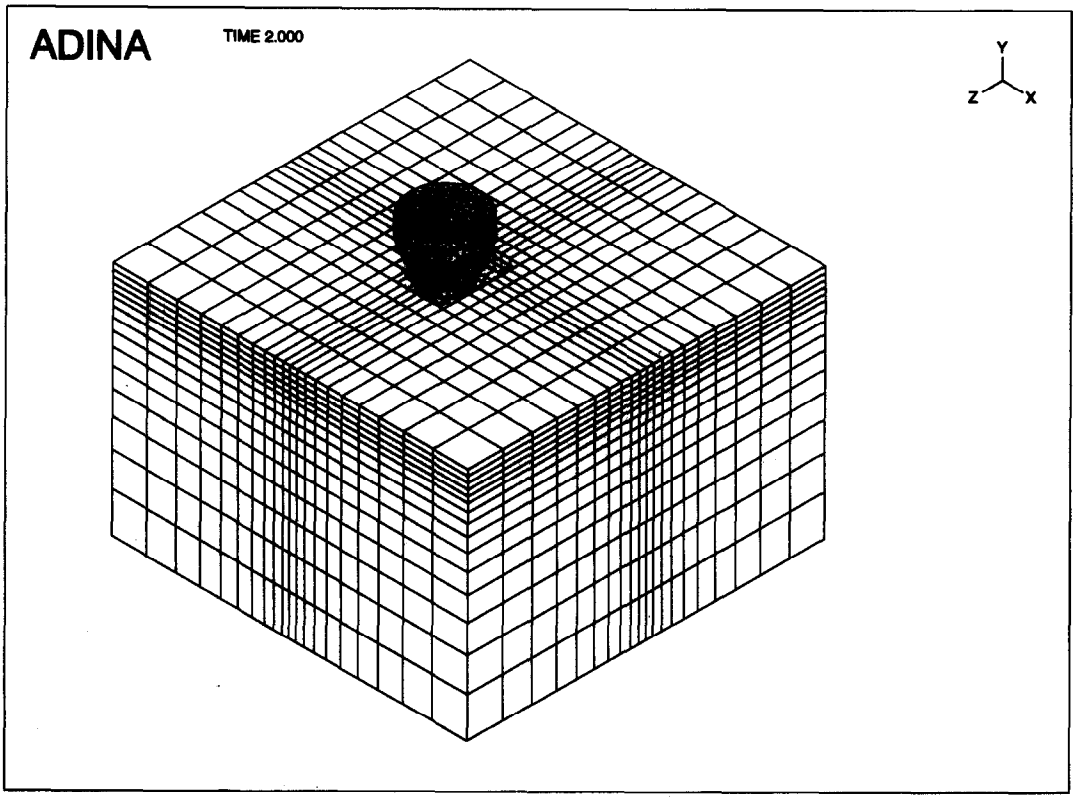

Fig. 14. Final configuration of tooth cutting into rock.

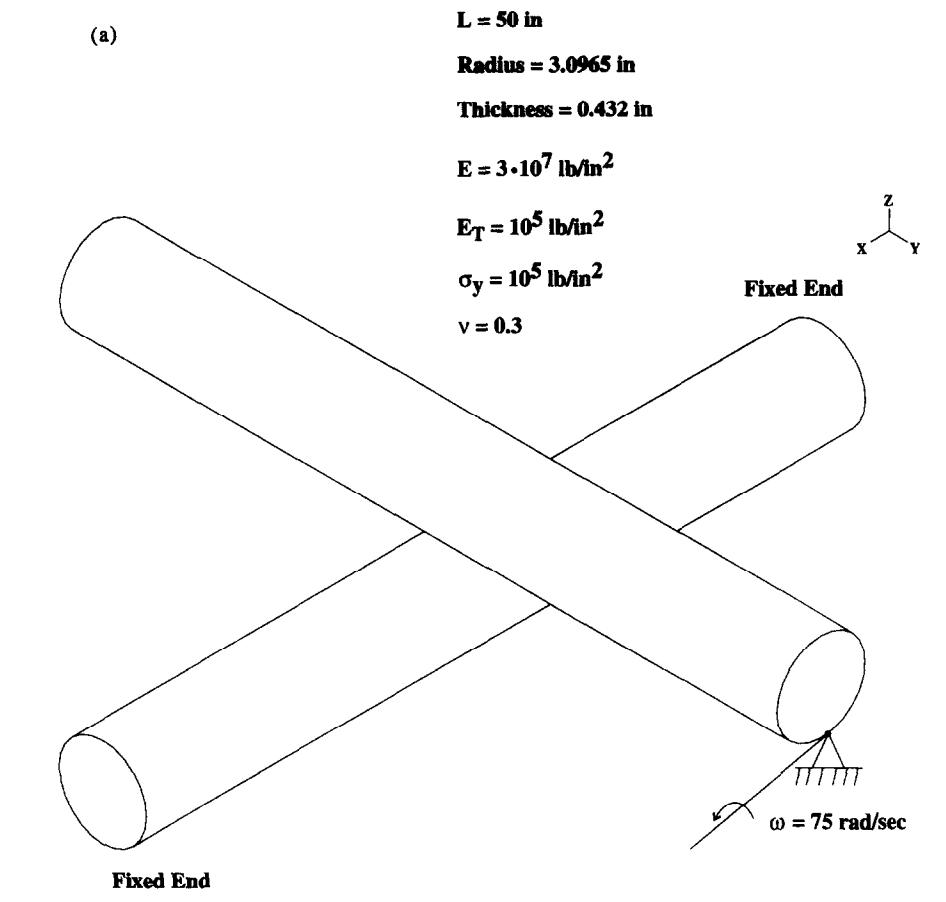

Fig. 15. Analysis of impact of two pipes: (a) problem considered; (b) finite element shell model.

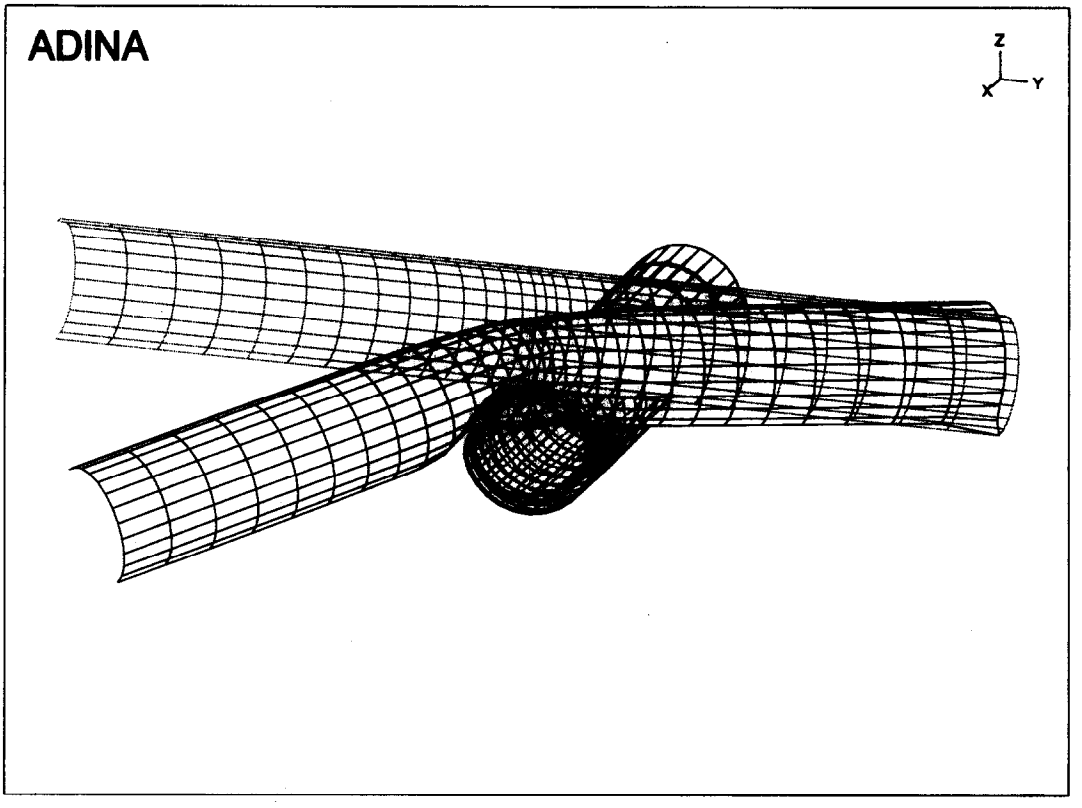

Fig. 16. Initial and final deformed configurations of pipes.

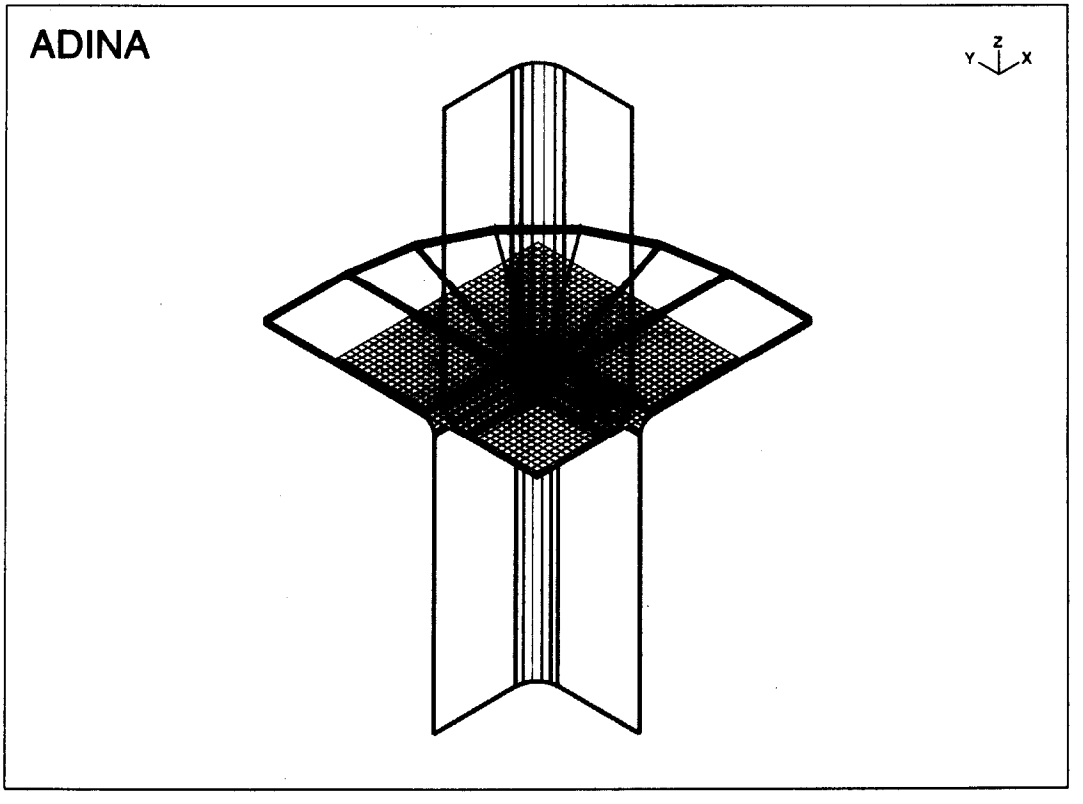

Fig. 17. Finite element model of sheet metal forming problem.

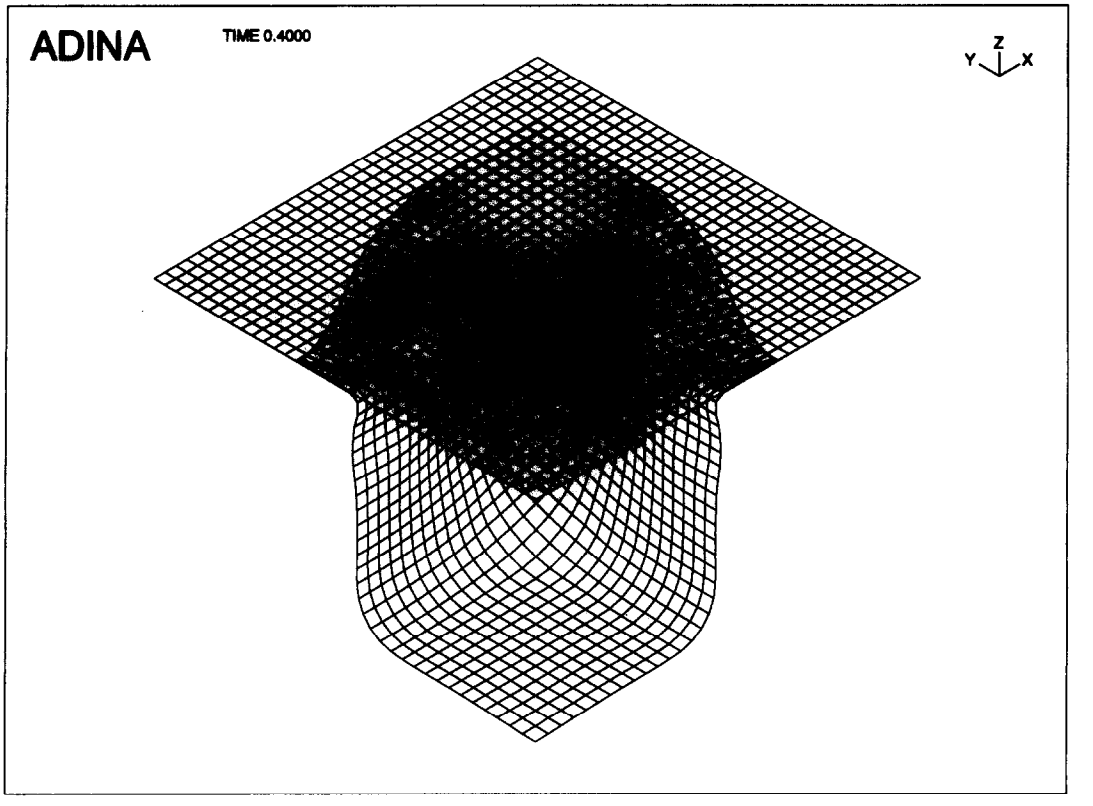

Fig. 18. Original sheet and deformed sheet in final configuration.

used with a time step $\Delta t = 5 \times 10^{-5}$ s and the special impact corrections. After the upper pipe rebounds, the maximum accumulated effective plastic strain is about 30%.

5.6. *Analysis of metal forming problem*

This is a benchmark square-cup deep-drawing problem described in Ref. [7]. The blank mild steel sheet has an initial size of 150 × 150 mm and an initial thickness of 0.78 mm. No friction is assumed in the solution. Only one quarter of the structure was discretized due to symmetry conditions. A mesh of 35 × 35 MITC4 shell elements was used for the blank (see Fig. 17).

The problem was solved with ADINA dynamically with (1) the implicit Newmark method and (2) the explicit central difference scheme. For the explicit solution, the material density was (artificially) chosen to be 10^6 times larger than the physical density in order to increase the stable time step value by a factor of one thousand. In the explicit algorithm, contact is enforced by simply satisfying the impact momentum change equations for the masses at the contactor and target surfaces together with the contact compatibility conditions.

To apply the 40 mm punch stroke, 4000 time steps were used in the explicit solution. Figure 18 shows the deformed state of the sheet at the maximum punch stroke. The explicit and implicit solutions give virtually the same results in deformations, with the explicit solution using about one-tenth of the solution time.

We should note that we did not endeavor to solve this problem in detail, and therefore do not give detailed solution results. Our only objective is to point out that explicit and implicit time integration solutions of metal forming problems can be obtained using a single computer program. In addition, a restart from explicit to implicit integration (or static analysis), or vice versa, can be directly performed. However, for an efficient explicit solution, the mass density or speed of forming process has to be increased considerably. The effect on the solution results of this artificial change from the actual physical conditions can be significant (see Ref. [5] for an example solution and study) and the implicit solution is clearly more reliable.

6. CONCLUSIONS

The objective in this paper was to review the theoretical basis of the constraint function method for contact problems and to present some solutions obtained with the method. We can conclude that the method is a very useful procedure to solve complex contact problems. The effectiveness of the method lies in the fact that constraint functions are employed that enforce the contact constraints. These functions are continuous and differentiable for any state of deformation. While we use the Lagrange multiplier

method to impose the constraint functions, a penalty method might be equally employed [1].

REFERENCES

1. Bathe, K. J., *Finite Element Procedures*. Prentice Hall, Englewood Cliffs, NJ, 1996.
2. Eterovic, A. L. and Bathe, K. J., On the treatment of inequality constraints arising from contact conditions in finite element analysis. *Computers and Structures*, 1991, **40**, 203–209.
3. Rabinowicz, E., *Friction and Wear of Materials*. Wiley, New York, 1996.
4. Oden, J. T. and Martins, J. A. C., Models and computational methods for dynamic friction phenomena. *Computer Methods in Applied Mechanics and Engineering*, 1985, **52**, 527–634.
5. Bathe, K. J., Guillermin, O., Walczak, J. and Chen, H., Advances in nonlinear finite element analysis of automobiles. *Computers and Structures*, 1997, **64**, 881–891.
6. Bathe, K. J. and Chaudhary, A. B., A solution method for planar and axisymmetric contact problems. *International Journal for Numerical Methods in Engineering*, 1985, **21**, 65–88.
7. Makinouchi, A., Nakamachi, E., Oñate, E. and Wagoner, R. H. (eds), In *Proceedings*, *NUMISHEET* '93, Isehara, Japan, 1993.